Buckling of epithelium growing under spherical confinement

Authors: Anastasiya Trushko[1], Ilaria Di Meglio[1], Aziza Merzouki[2], Carles Blanch-Mercader[1,3], Shada Abuhattum[4,5], Jochen Guck[4], Kevin Alessandri[6], Pierre Nassoy[6], Karsten Kruse[1,3,7], Bastien Chopard[2], Aurélien Roux[1,7,*]

Affiliations:

[1]department of Biochemistry, University of Geneva, CH-1211 Geneva, Switzerland.
[2]department of Computer Science, University of Geneva, CH-1211 Geneva, Switzerland.
[3]department of Theoretical Physics, University of Geneva, CH-1211 Geneva, Switzerland.
[4]Biotechnology Center, Technische Universität Dresden, D-01307 Dresden, Germany.
[5]JPK Instruments AG, 12099 Berlin, Germany
[6]Université de Bordeaux, Laboratoire Photonique Numérique et Nanosciences & CNRS and Institut d'Optique, LP2N, UMR 5298, F-33400, Talence, France.
[7]National Center of Competence in Research Chemical Biology, University of Geneva, CH-1211 Geneva, Switzerland.

*Correspondence to: Aurelien.Roux@unige.ch

Abstract: Many organs, such as the gut or the spine are formed through folding of an epithelium. Whereas genetic regulation of epithelium folding has been investigated extensively, the nature of the mechanical forces driving this process remain largely unknown. Here we show that monolayers of identical cells proliferating on the inner surface of elastic spherical shells can spontaneously fold. By measuring the elastic deformation of the shell we inferred the forces acting within the monolayer. Using analytical and numerical theories at different scales, we found that the compressive stresses arising within the cell monolayer through proliferation quantitatively account for the shape of folds observed in experiments. Our study shows that forces arising from epithelium growth are sufficient to drive folding by buckling.

One Sentence Summary: Epithelial cells proliferating in an artificial, elastic hollow sphere accumulate compressive stresses that drive inward buckling.

Main Text:

Epithelium folding is essential for the formation of many organs, such as the gut during gastrulation and the central nervous system during neurulation (*1-2*). There are three major mechanisms driving invaginations: convergent extension, apical constriction, and cellular flows (*1-3-4*), which contribution to epithelial folding is however difficult to evaluate in vivo. Alternatively, theoretical studies proposed that cell proliferation in confined geometries induce epithelium folding through buckling (*5-8*). Buckling is a bending instability occurring in elastic material under compressive forces (*9*).

To test if forces generated by proliferation can induce spontaneous buckling of epithelia, we undertook an in vitro approach and studied the proliferation of epithelial cells confined in a

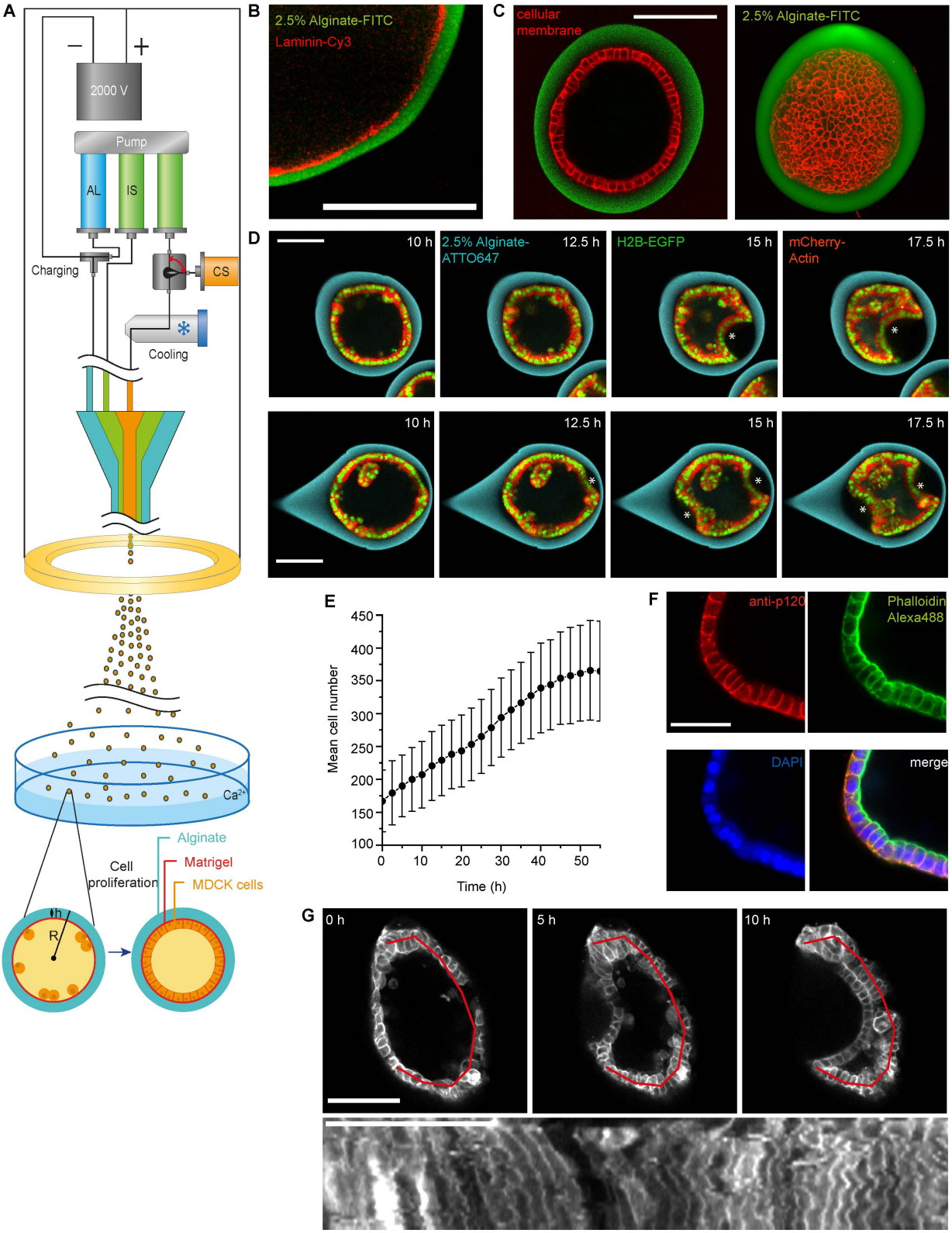

Fig. 1. Characterization of epithelium growth and folding in a spherical capsule. (**A**) Schematic of experimental setup (see also Fig S1). (**B**) Confocal equatorial plane of an alginate capsule and Matrigel (Cy3-Laminin). (**C**) Left, confocal plane and right, maximum Z-projection of a fully formed MDCK spherical monolayer. Red, deep-red CellMask (thermofisher). (**D**) Confocal equatorial planes of one fold (top) and two folds (bottom) of epithelium. (**E**) Mean cell number per capsule over time; 3 exps, N=53 capsules; error bars are SDs. (**F**) Polarity of a formed fixed, immunostained monolayer: anti-p120 (baso-lateral), phalloidin-Alexa488 (apical). (**G**) Top; Confocal equatorial planes of Myr-

PALM-GFP-MDCK monolayer during folding. T=0 is when folding starts. Bottom; Kymograph along the red line shown above 10h post-folding. Time is towards the bottom, Scale bars, 100 µm.

spherical shell. The spherical geometry presents several advantages over others: it is the one of early embryos, without boundaries, such that all cells experience the same environment. Specifically, we encapsulated MDCK- II cells in hollow alginate spheres, hereon referred to as capsules. To form them, we used a 3D-printed microfluidic device to generate three-layered droplets, which outer layer made of alginate undergoes gelation when falling in 100mM $CaCl_2$ solution (Fig 1A, Fig S1 and methods)(*10-11*). The inner surface of the capsules is coated with a 3-4 µm thick layer of Matrigel to which cells adhere (Fig 1B)(*10*).

Encapsulated cells were imaged using 3D time-lapse confocal microscopy. Time zero corresponds to the start of imaging, 24h after capsules formation (Methods). Initially, MDCK-II cells were sparsely distributed on the capsule's inner surface. Through proliferation, cells first formed clusters, which then merged into a monolayer (Fig 1C and Fig S2). Monolayers reached confluency at 8.8±0.8 hours (mean±SEM, as in the rest of the text, unless noted, N=54). Strikingly, monolayers folded after 14.5±0.8 hours (N=54) in approx. 80-90% of the capsules. In this process, a portion of the monolayer detached from the alginate shell and bent inwards (Fig 1D and Fig S3, SI Movie1). Proliferation was unaffected by confluency or folding, as the cell number increased linearly with a rate of 3.6±0.1 cells per hour (N=54) during 55 hours (Fig 1E). We concluded that a cell monolayer proliferating inside a spherical shell can fold similarly to embryonic epithelia during development.

To understand the driving mechanism of folding, we first checked that confinement was essential. Capsules were dissolved using alginase prior to folding and no monolayer folding was observed (Fig S3). Furthermore, as the apical side faced the interior of capsules (Fig 1F), apical constriction would rather oppose than promote folding in our system (*4-7-12-13*). In addition, no large-scale collective cellular flows were observed (Fig 1G). These observations show that neither apical constriction nor cellular flows can cause folding in our system. We then tested the last possibility that folding occurred through buckling.

Buckling is driven by compressive stresses in the monolayer. Since alginate is elastic, stresses caused by proliferating cells can be inferred from its deformations. Notably, proliferation of the monolayer generated pressure resulting in capsule wall thinning (Fig 2A). Detecting contours of capsules from confocal images (Fig 2D & 2C), the averaged wall thickness with time was measured for four different alginate concentrations (1, 1.5, 2, and 2.5%, see methods, Fig S4 and Fig 2D). Capsules without cells kept constant wall thickness (Fig S4). We used empty capsules to measure the Young modulus of alginate by atomic force microscopy (AFM) (methods and Fig 2E)(*14*). From the wall thickness and the Young modulus, the pressure exerted on capsules by cells over time can be calculated (methods and Fig 2F). For all

alginate concentrations, the pressure increased during approx. 55h, reaching a plateau around 300-400 Pa. We concluded that compressive stresses corresponding to pressures below 300 Pa had no significant impact on the proliferation rate (Fig 1E).

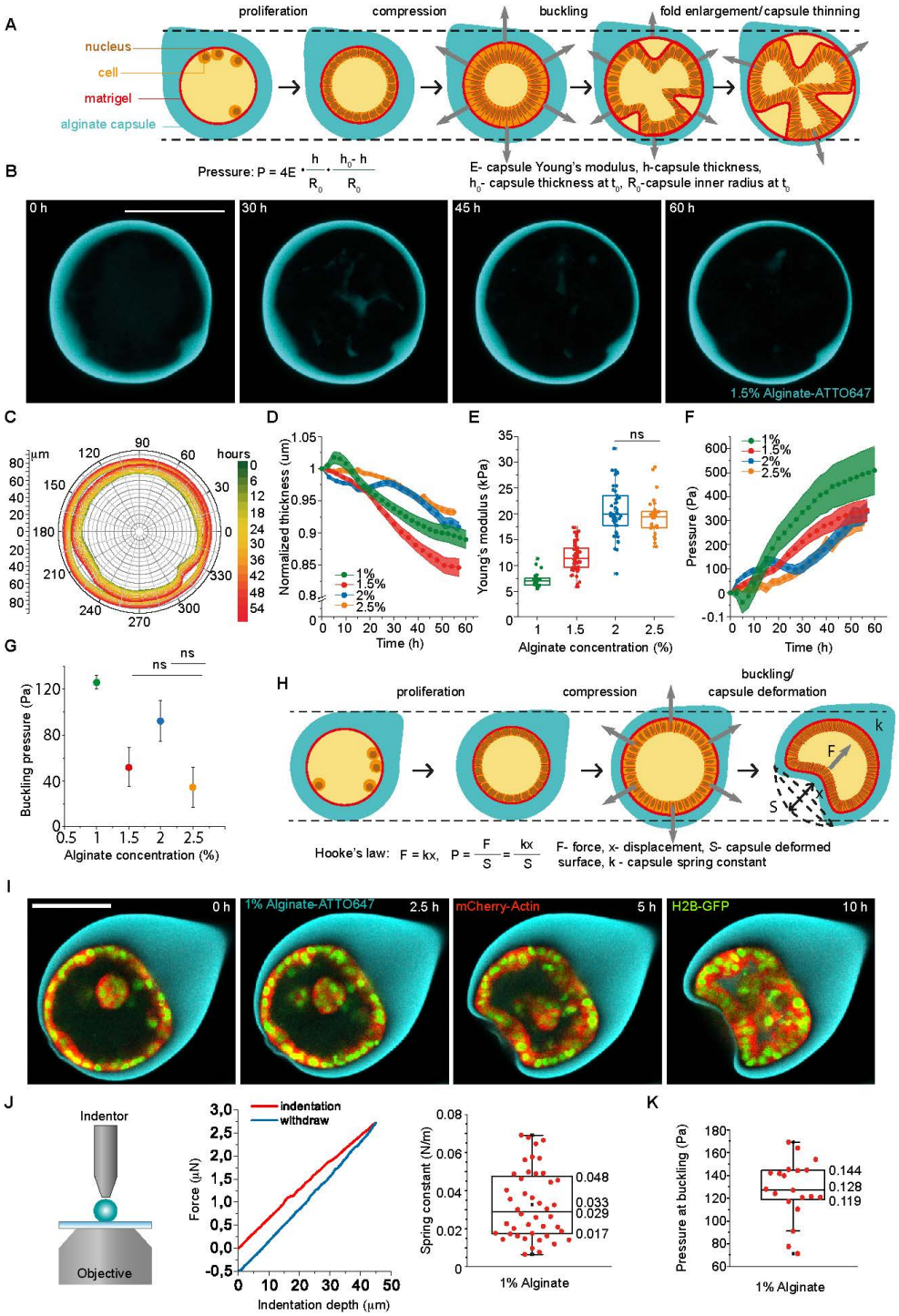

Fig. 2. Pressure measurements by elastic deformation of the alginate wall. (**A**) Schematic of capsule thinning during epithelium proliferation. (**B**) Confocal equatorial plane of thinning alginate capsule. (**C**) Superimposed contours of inner and outer boundaries corresponding to different time points. (**D**) Normalized mean capsule thickness as a function of time for different alginate concentrations. (**E**) Young's modulus (kPa) as a function of the alginate concentration measured by AFM. Respective Young moduli are: 1%, 7.1±0.3 kPa (N=25), 1.5%, 11.5±0.4 kPa (N=52), 2%, 20.7±0.7 kPa (N=46) and 2.5%, 19.5±0.7 kPa (N=29). (**F**) Evolution of pressure (Pa) within capsules over time during epithelium proliferation and for different alginate concentrations. (**G**) Mean buckling

pressure (Pa) for different alginate concentration. For d, f, and g: 1% alginate, n=22; for 1.5%, n=35; for 2%, n=25; for 2.5%, n=53; error bars are SEM. (**H**) Schematic of capsule invagination following epithelium folding. (**I**) Confocal equatorial planes showing capsule invagination for 1% alginate capsule. (**J**) Left, schematic of an indentation experiment with the FemtoTools indenter (see also Fig S4). Right, a representative plot of force with indentation depth.. (**K**) Box plot of spring constant for 1% alginate. (**L**) Box plot of pressure at buckling (Pa) for 1% alginate capsule calculated from capsule deformation. Scale bars, 100 μm.

Importantly, at the time of folding (approximately 14.5h), cell proliferation rate remained constant. Upon folding, the pressure was between 50 and 100 Pa for 1.5, 2 and 2.5% alginate concentration (Fig 2G). For 1%, the force exerted by cells onto the alginate shell was estimated by Hooke's law from the deflection of the capsule and its stiffness (Fig 2H, SI Movie 2). The capsule stiffness (0.03±0.003 N/m, N=44, Fig 2K) was measured using an FT-S100 indenter (FemtoTools, Buchs, Switzerland, see methods, Fig S4 and Fig 2J). The average deflection force was 1.8±0.2 μN (N=20). Dividing this value by the invagination area, we obtained a pressure of 128±6 Pa (N=20) (Fig 2L), of the same order than for other alginate concentrations (Fig 2G). Our results show that monolayer folding occurred at a pressure of approx. 100 Pa, which is independent of alginate stiffness.

Next, we determined the corresponding compressive stress within the monolayer. To this end, we used a continuum theoretical description, without cellular details. The cell monolayer is described as a circular elastic ring, reproducing the geometry found on equatorial confocal planes (Fig 3A). The so-called cellular ring has a radius r if it is not confined. Two elastic parameters characterize its mechanics: the bending rigidity $\mathcal{K}$ and the compressional rigidity λ (SI). Confinement is accounted for by restricting the cellular ring to a circular domain of radius R. For $r>R$, confinement is achieved by a harmonic spring of constant k. Hence, the total energy is a combination of the bending, compression, and confinement energies (SI). From now on, we consider the realistic limit $\mathcal{K}/\lambda R^2 \ll 1$ and $\lambda/kR^2 \ll 1$, meaning that compression is energetically favored over bending and that the confinement is rigid (SI).

This system exhibits a first order buckling transition controlled by the excess strain $\Delta\varepsilon=\Delta L/2\pi R$ (*15-16*), with the excess length $\Delta L=2\pi(r-R)$ (Fig 3B and SI). The threshold excess strain at the transition can be deduced by comparing the energies in the two limiting cases of a compressed unbuckled ring (Fig 3C) and of an uncompressed buckled ring (Fig 3D). The buckling transition occurs when the buckled ring energy equals the compressed ring energy, leading to a threshold excess strain $\Delta\varepsilon_c \sim (\mathcal{K}/\lambda R^2)^{3/5}$ that depends on both the tissue material properties and the confinement geometry.

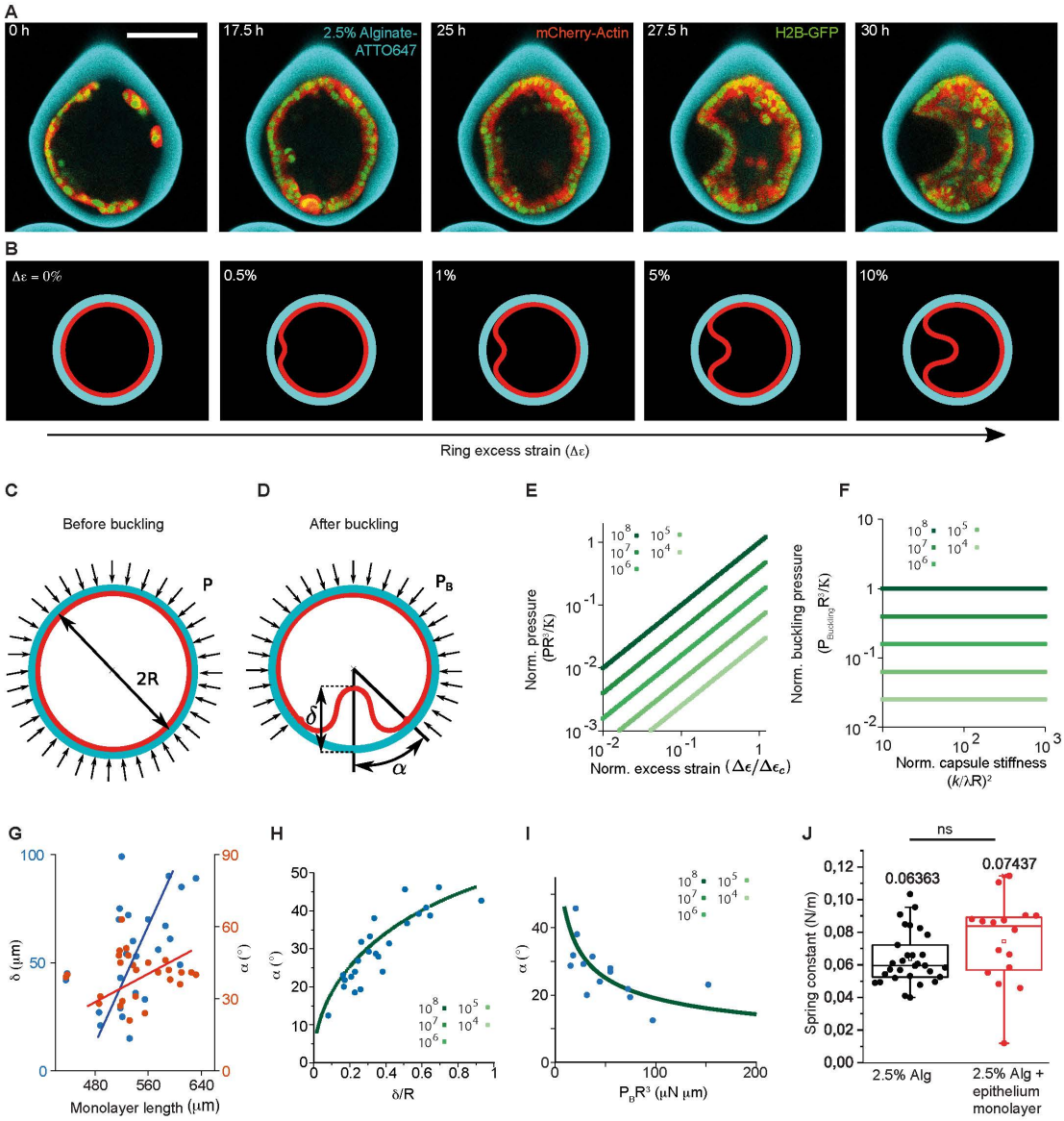

Fig. 3. Continuum theory of the buckling transition and comparison to experimental data. (**A**) Confocal equatorial planes of epithelial monolayer bending. (**B**) Equilibrium shapes of a buckled elastic ring (red) under circular confinement (cyan) as a function of ring excess strain (Δε), calculated from continuum theory (see text and SI). (**C**) Schematic of a compressed elastic ring (red) under the pressure P of the confinement ring (cyan). (**D**) Schematic of a buckled elastic ring (red) under the pressure P_B of the confinement ring (cyan). (**E**) Normalized pressure ($PR^3/\mathcal{K}$) as a function of the normalized excess strain at the buckling instability (Eq. (S17) in SI) for values of the normalized compressional rigidity ($\lambda R^2/\mathcal{K}$) between 10^4 and 10^8. (**F**) Normalized buckling pressure ($P_{buckling}R^3/\mathcal{K}$) as a function of the normalized capsule stiffness ($k/\lambda R^2$) for compressional rigidity values in panel **E**. (**G**) Experimental values of δ and α as a function of the length of one-folded epithelia. Solid lines are guides to the eyes, not fits. (**H**) Blue dots, experimental values (δ,α) from panel **G**. Green solid lines, theoretical relation between δ and α for the compressional rigidity values in panel **E**. (**I**) Blue dots, experimental values (α,$P_B R^3$) from panel **G**. Only dots where δ was smaller than R were kept for the fit. Solid green lines: fits to the theoretical relation between α and P_BR^3 giving $\mathcal{K}$=1.2 μN.μm. (**J**) Spring constant values of 2.5% alginate capsules with and without a cell monolayer (see Fig S4).

From this, the pressure at buckling can be determined. Below the threshold ($\Delta\varepsilon<\Delta\varepsilon_c$), the cell ring compression is stabilized by a uniform pressure P exerted by the confinement (Fig 3C). The energy associated with this pressure is $\sim PR^2\Delta\varepsilon$ and equals the ring compression energy $\Delta E\sim\lambda R\Delta\varepsilon^2$, yielding $P\sim\lambda\Delta\varepsilon/R$ (Fig 3E). Hence, the pressure at the buckling transition $P_{buckling}$, when $\Delta\varepsilon\sim\Delta\varepsilon_c$,

$$P_{\text{buckling}}\sim \lambda^{2/5}\mathcal{K}^{3/5}/R^{11/5}\boxed{P_{buckling}\sim \lambda^{2/5}K^{3/5}/R^{11/5}} \quad (1)$$

depends only on the material properties of the monolayer and on the capsule geometry, but not on the capsule stiffness k (Fig 3F), in agreement with our experimental observations (Fig 2G,K). Above the threshold ($\Delta\varepsilon>\Delta\varepsilon_c$), the buckled ring is stabilized by a uniform pressure P_B on the undeformed ring segment (Fig 3D and SI). P_B can be expressed in terms of α and δ and independent of λ (*16*) (SI). α, δ, and P_B can be experimentally measured in capsules with a single fold (Fig 3G). The dependence of α with δ fulfils theoretical prediction with no other free parameter (Fig 3H), supporting that the folded monolayer's shape emerges from buckling.

We then wondered how single cell properties could participate to the buckling transition. To this end, we numerically analyzed the cell monolayer dynamics inside alginate capsules using a 2D vertex model (*6-8-17-18*). When simulations start, cells are characterized by a resting area $A^0 = 300\mu m^2$and a resting edge length L^0, with $(L^0)^2 = A^0$ (SI and Fig 4A). Deviations from these values are penalized by harmonic spring energy terms with constants K and k^s for the area and the length, respectively (Fig 4A and SI) (*17-19*). In addition, large bending deformations of the monolayer are penalized by a harmonic spring energy term with constant c^b (SI). K, the cell elasticity, can be estimated by $K\sim\lambda/A_0\sim10^9$ N/m^3. As in the continuum theory, the monolayer is confined to a circular domain of radius R by a spring constant $k = 0.06N/m$ (SI).

To simulate proliferation, cells stochastically divide with a probability $p_{mitosis}$ (SI). Simulations started with 40 cells, similar to the cell number in a confocal section at confluency, and ended when the cell number doubled. Simulations reproduced folding (Fig 4B, SI Movie 3). The monolayer pressure grew continuously over time before and after buckling as in experiments (Fig 4C). However, the continuum theory predicts that pressure after buckling decreases as the excess strain increases (SI). Thus, proliferation accounts for the pressure dynamics in experiments.

Strikingly, we found that simulation folds acquired budded shapes unlike to experiments, owing to cell flows towards the fold's neck (Fig 4D). We reasoned that in experiments, cell adhesion to the Matrigel acts as an effective friction (Fig 1G). We found that a friction force $F_{NS}\sim5.10^{-3}\mu N$ in simulations prevents cell lateral displacements on the capsule's inner surface and fold necks stayed wide, resembling experimental shapes (Figs 4E-1D, SI Movie 4).

We next wondered which cell parameters set the number and positions of folds (Fig 4F-H). In experiments, two folds is the most frequent case (50%) followed by one fold (20%) (Fig 4G). This is different from the continuum theory, where equilibrium shapes feature a single fold (SI). In case of two folds, angles between folds were between 150° and 180°, whereas in case of three

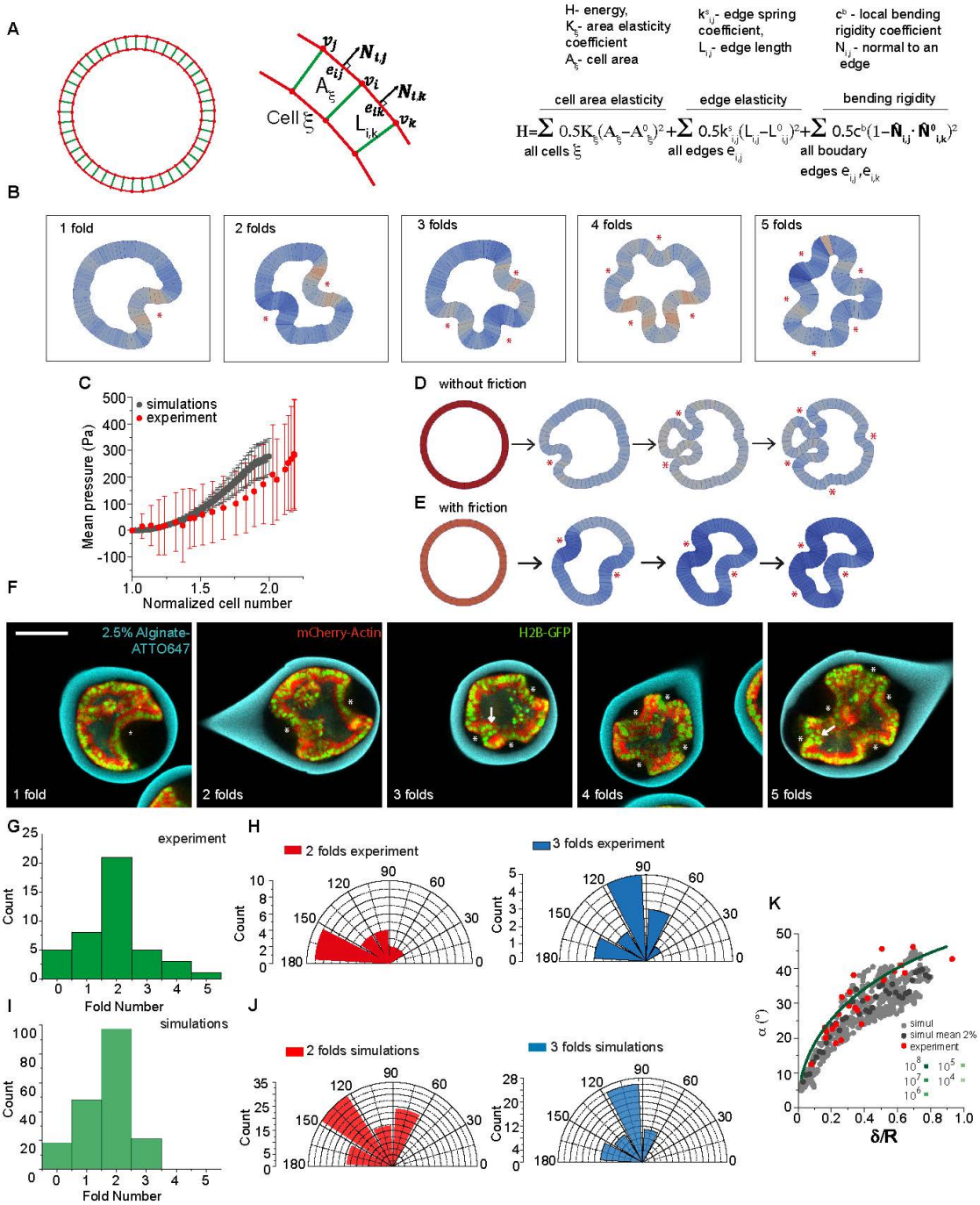

Fig. 4. Dynamic simulations of epithelial growth and buckling. (A) Theoretical model for numerical simulations. **(B)** Representative ending shapes of simulations executed with different couples of (c^b,k^s). Asterisks show folds. **(C)** Mean pressure as a function of cell number in experiments (n=53 capsules) and *in silico* (n=184)*;* error bars are SDs. **(D)** Shape evolution of a cell ring simulated using the same sequence than in e, but without friction force. **(E)** Shape evolution of a cell ring simulated using the same sequence as in D, but with friction force $F_{NS} = 5.10^{-3}\mu N$. **(F)** Representative confocal equatorial planes of MDCK monolayer with 1 to 5 folds. Asterisks show folds. Arrows show high curved folds.

Scale bar 100µm. **(G)** Histogram of fold number for 2.5% alginate capsules. **(H)** Angle distribution between consecutive folds for 2 (red) and 3 (blue) folds in 2.5% alginate capsules. **(I)** Histogram of fold number obtained *in silico* for $k^S/c^b = 3.3\ 10^{-8}$. **(J)** Angle distribution between consecutive folds for 2 (red) and 3 (blue) folds *in silico* for $k^S/c^b = 3.3\ 10^{-8}$. **(K)** α as function of δ/R obtained from experiments (red), continuum theory (green line) and simulations (grey and dark grey points).

folds, they were between 90° and 120° (Fig 4H). In simulations, we search for parameter values that reproduce these experimental observations. A shape diagram (SI and Fig S9) shows that along the line $k^S/c^b = 3.3\ 10^{-8}$, the fold number (Fig 4I) and angle distributions (Fig 4J) were similar to experiments (Fig 4G,H). Moreover, the shape of folds obtained in these simulations matched the ones observed in experiments and continuum theory, as seen from the relation between α and δ (Fig 4K-3H). To find realistic values of k^S and c^b, we used parameter sets for which the pressure at buckling would match experimental values (Fig 2F and 2G), yielding to $k^s \sim 3.10^{-3} N/m$ and $c^b \sim 9\ \mu N.\mu m$ with buckling occurred between 90 and 180 Pa (SI). It shows that, in addition to proliferation and friction, cell mechanics played essential roles in controlling shape, number and distribution of monolayer folds.

In this study, we show that an epithelium growing under spherical confinement buckles due to the compressive stresses arising from cell proliferation. The pressure necessary for epithelium buckling is at least five times lower than that required to hinder cell proliferation. Our study adds to the mechanical processes described in vitro to play a role in tissue folding through proliferation, from mesenchymal constriction (*20*) to constrained heterogeneous growth (*21-22*). It also strengthens the concept that unique physical properties of cells are required during morphogenesis, like superelasticity during growth of epithelium domes (*23-24*), or liquid to solid phase transition during elongation of the fish embryo (*25*). Our in vitro findings establish a buckling mechanism that could participate in many epithelium folding events occurring during embryogenesis.

References and Notes:

1. L. A. Davidson, Epithelial machines that shape the embryo. *Trends in Cell Biology* **22**, 82-87 (2012).
2. T. Lecuit, P. F. Lenne, E. Munro, Force generation, transmission, and integration during cell and tissue morphogenesis. *Annu Rev Cell Dev Biol* **27**, 157-184 (2011).
3. T. J. C. Harris, Sculpting epithelia with planar polarized actomyosin networks: Principles from Drosophila. *Semin Cell Dev Biol*, (2017).
4. T. Lecuit, P. F. Lenne, Cell surface mechanics and the control of cell shape, tissue patterns and morphogenesis. *Nat Rev Mol Cell Biol* **8**, 633-644 (2007).
5. E. Hannezo, J. Prost, J. F. Joanny, Theory of epithelial sheet morphology in three dimensions. *Proc Natl Acad Sci U S A* **111**, 27-32 (2014).
6. A. Hocevar Brezavscek, M. Rauzi, M. Leptin, P. Ziherl, A model of epithelial invagination driven by collective mechanics of identical cells. *Biophys J* **103**, 1069-1077 (2012).
7. M. Krajnc, P. Ziherl, Theory of epithelial elasticity. *Phys Rev E Stat Nonlin Soft Matter Phys* **92**, 052713 (2015).
8. M. Rauzi *et al.*, Embryo-scale tissue mechanics during Drosophila gastrulation movements. *Nat Commun* **6**, 8677 (2015).
9. L. Landau, E. Lifshitz, Elasticity theory. (1975).

10. K. Alessandri *et al.*, A 3D printed microfluidic device for production of functionalized hydrogel microcapsules for culture and differentiation of human Neuronal Stem Cells (hNSC). *Lab Chip* **16**, 1593-1604 (2016).
11. K. Alessandri *et al.*, Cellular capsules as a tool for multicellular spheroid production and for investigating the mechanics of tumor progression in vitro. *Proc Natl Acad Sci U S A* **110**, 14843-14848 (2013).
12. M. D. Diaz-de-la-Loza *et al.*, Apical and Basal Matrix Remodeling Control Epithelial Morphogenesis. *Dev Cell* **46**, 23-39 e25 (2018).
13. N. Storgel, M. Krajnc, P. Mrak, J. Strus, P. Ziherl, Quantitative Morphology of Epithelial Folds. *Biophys J* **110**, 269-277 (2016).
14. I. N. Sneddon, The relation between load and penetration in the axisymmetric boussinesq problem for a punch of arbitrary profile. *Int J Eng Sci* **3**, 47-57 (1965).
15. H. Lo, J. Bogdanoff, J. Goldberg, R. Crawford, in *the fourth U.S. National Congress of Applied Mechanics* (American Society of Mechanical Engineers, New York, 1962), pp. 691-695.
16. H. Chan, S. McMinn, The stability of a uniformly compressed ring surrounded by a rigid circular surface. *International Journal of Mechanical Sciences* **8**, 433-442 (1966).
17. A. Merzouki, O. Malaspinas, B. Chopard, The mechanical properties of a cell-based numerical model of epithelium. *Soft Matter* **12**, 4745-4754 (2016).
18. A. Merzouki, O. Malaspinas, A. Trushko, A. Roux, B. Chopard, Influence of cell mechanics and proliferation on the buckling or simulated tisues using a vertex model. *Natural Computing*, (2017).
19. B. R. Bruckner, H. Noding, A. Janshoff, Viscoelastic Properties of Confluent MDCK II Cells Obtained from Force Cycle Experiments. *Biophys J* **112**, 724-735 (2017).
20. A. J. Hughes *et al.*, Engineered Tissue Folding by Mechanical Compaction of the Mesenchyme. *Dev Cell* **44**, 165-178 e166 (2018).
21. T. Savin *et al.*, On the growth and form of the gut. *Nature* **476**, 57-62 (2011).
22. T. Tallinen, J. Y. Chung, J. S. Biggins, L. Mahadevan, Gyrification from constrained cortical expansion. *Proc Natl Acad Sci U S A* **111**, 12667-12672 (2014).
23. E. Latorre *et al.*, Active superelasticity in three-dimensional epithelia of controlled shape. *Nature*, (2018).
24. P. Fernandez, A. Ott, Single cell mechanics: stress stiffening and kinematic hardening. *Phys Rev Lett* **100**, 238102 (2008).
25. A. Mongera *et al.*, A fluid-to-solid jamming transition underlies vertebrate body axis elongation. *Nature* **561**, 401-405 (2018).

Acknowledgements:

Authors thank Oresti Malaspinas for his useful insights into the project. **Funding:** AR and BC acknowledge funding from the SystemsX EpiPhysX consortium. AR acknowledges funding from Human Frontier Science Program Young Investigator Grant RGY0076/2009-C, the Swiss National Fund for Research Grants N°31003A_130520, N°31003A_149975 and N°31003A_173087, and the European Research Council Consolidator Grant N° 311536. IDM and AR acknowledge funding from Secrétariat d'Etat à la Recherche et à l'Innovation grant agreement REF-1131-52107. I.D.M., S.A., A.R. and J.G. acknowledge funding from the EU Horizon2020 Marie Sklodowska-Curie ITN "BIOPOL" (grant agreement No 641639).

Author contributions: A.T. and A.R. designed the project; A.T. performed all experiments and image analyzes, with exception of cell proliferation measurements; I.D.M. helped with capsule formation, 4D confocal imaging, and performed cell proliferation measurements. K.A. and P.N. designed and fabricated microfluidic devices, and optimized the encapsulation technology. A.M. and B.C. designed numerical simulations, and A.M. performed them. C.B-M. and K.K. developed continuum theory. S.A. and J.G. measured Young's moduli of capsules by AFM.

A.T., I.D.M., C.B-M, A.M., B.C., K.K. and A.R. analyzed the results, and wrote the paper, with editions from other co-authors.